*Article*

# Computational Study of Cresyl Violet Covalently Attached to the Silane Coupling Agents: Application to TiO$_2$-Based Photocatalysts and Dye-Sensitized Solar Cells

**Tatsuya Takeshita**

Department of Applied Chemistry and Food Science, Fukui University of Technology, 3-6-1 Gakuen, Fukui 910-8505, Japan; takeshita@fukui-ut.ac.jp

check for updates

**Abstract:** The covalent attachment of photosensitizing dyes to TiO$_2$ using silane coupling agents (SCAs) is a promising strategy for enhancing the photocatalytic activity of TiO$_2$-based photocatalysts and the photovoltaic conversion of dye-sensitized solar cells (DSSCs). This approach can control the geometry and orientation of the photosensitizing dye on the TiO$_2$ surface. In this study, a density functional theory (DFT) and time-dependent DFT (TD-DFT) investigation was carried out on cresyl violet (CV) covalently attached to SCAs with a terminal oxirane group (OTES–Cn) to reveal the influence of OTES–Cn on the geometry of the photosensitizing dyes. The potential of CV covalently attached to OTES–Cn (CV–OTES–Cn) to act as a photosensitizing dye was also analyzed. The hydroxyl group formed by the epoxy-opening reaction between CV and OTES–Cn strongly influenced the geometry of CV–OTES–Cn, which was attributed to a CH–O interaction. Additionally, TD-DFT, frontier molecular orbital and molecular electrostatic potential calculations revealed that CV–OTES–Cn has excellent optical properties and electron injection ability. In particular, the characteristics of the unbent conformation of CV–OTES–Cn are expected to contribute significantly to the photocurrent in TiO$_2$-based photocatalysts and DSSCs. These findings enhance the understanding of the covalent attachment strategy using SCAs and contribute to improving TiO$_2$-based photocatalysts and DSSCs.

**Keywords:** cresyl violet; silane coupling agents; titanium dioxide; photocatalysts; dye-sensitized solar cell; DFT and TD-TDF calculation

## 1. Introduction

Photoredox catalysts play an essential role in various fields, including environmental remediation, solar energy conversion and organic photochemistry [1–3]. Titanium dioxide (TiO$_2$) is a typical photoredox catalyst with strong oxidation and reduction abilities [4]. Generally, TiO$_2$ exhibits photocatalytic behavior under UV light with a photon energy corresponding to the bandgap between its conduction band (CB) and valence band levels. Hence, modification is required to enhance its photocatalytic activity and absorb visible light, as the UV region represents only ~4% of the solar spectrum [5,6].

Surface and interface modifications are useful strategies for fabricating visible-light-responsive TiO$_2$. In particular, the chemical adsorption of organic dyes onto the surface of TiO$_2$ is a simple method to impart it with a visible light response; the photosensitization occurs via electron injection from the adsorbed organic dyes into the CB of TiO$_2$. Using this strategy, dye-sensitized solar cells (DSSCs), which are one of the main applications of TiO$_2$, with a photovoltaic conversion efficiency (PCE) of 14.3% have been achieved [2].

In addition to the photosensitizing dye's visible light response, the dye's geometry on the $TiO_2$ surface also strongly affects the electron injection efficiency. Improving the photosensitizing dye orientation can reduce unwanted electron transfer between dye molecules, which occurs due to aggregation of the dye and back-electron transfer between the oxidized dye and the electrons injected into $TiO_2$ [7,8].

In the design and synthesis of photosensitizing dyes, most investigations of methods to improve the dye's orientation on the $TiO_2$ surface have focused on attaching anchor groups to the dye [7–9]. However, most photosensitizing dyes have complex molecular structures designed to improve their optical properties (extended π-conjugation, push–pull structures, etc.) [2,10–12]. Adding anchor groups to these dyes to improve their orientation requires multiple synthetic steps and can be expensive.

Silane coupling agents (SCAs) consist of an alkyl alkoxysilane moiety and two or more different functional groups that enable the SCAs to covalently attach to both inorganic and organic materials [13,14]. Because SCAs can anchor photosensitizing dyes to the $TiO_2$ surface, they represent an easy and low-cost covalent-attachment strategy that can be used to enhance $TiO_2$-based photocatalysis and the PCEs of DSSCs [1,6,15]. Recently, Lu et al. reported improvement of the visible photocatalytic activity of $TiO_2$ using glycidoxypropyltrimethoxy silane and zinc (II) tetra-[α-(*p*-amino)benzyloxyl]phthalocyanine [1]. This strategy has also been applied to DSSCs [16,17]. Zamborini et al. reported that the stability of a DSSC was improved by using 3-aminopropyltriethoxysilane [16].

In addition to covalently linking inorganic and organic materials, SCAs can also form self-assembled monolayers (SAMs), attributed to the formation of a siloxane network [13,14]. The aligned orientation of these SAMs could be exploited to control a photosensitizing dye's geometry and orientation on a $TiO_2$ surface. Thus, understanding the geometry and characteristics of photosensitizing dyes covalently attached to SCAs is essential to enhance further the photocatalytic activity of $TiO_2$-based photocatalysts and the PCEs of DSSCs.

This article reports a density functional theory (DFT) and time-dependent DFT (TD-DFT) study of cresyl violet (CV, Figure 1) covalently attached to SCAs with a terminal oxirane group (OTES–Cn, Figure S1; Cn denotes the number of carbons in the alkyl chain, *n* = 2, 4 or 8). DFT and TD-DFT are powerful tools for understanding the geometry and characteristics of molecules. CV was chosen as the photosensitizing dye in this study based on its excellent optical properties. It contains an amino group that can form a covalent bond with an oxirane via an epoxy-ring-opening reaction between the amino and epoxy groups. Additionally, phenoxazine-based dyes are known to show high performance in DSSCs [18–20]. To the best of the author's knowledge, this is the first investigation of the combination of CV and OTES–Cn. This investigation will reveal both the influence of OTES–Cn on the geometry of photosensitizing dyes and CV's potential to attach to OTES–Cn covalently (CV–OTES–Cn) and act as a photosensitizing dye.
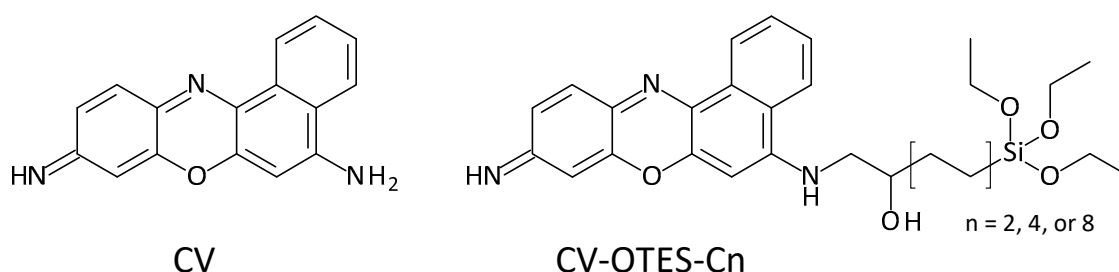


**Figure 1.** Chemical structures of cresyl violet (9-iminobenzo[a]phenoxazin-5-amine; CV) and CV–OTES–Cn. For the chemical structures of OTES–Cn, see Figure S1.

## 2. Computational Methods

Geometry optimization, frontier molecular orbital (FMO), UV-visible absorption spectrum simulation, frequency analysis and molecular electrostatic potential (MEP) calculations were carried

out using the Gaussian 09W package (Gaussian, Inc., Wallingford, CT, USA). The density of state (DOS) spectra were obtained using GaussSum (3.0.2) [21]. The geometries of all dyes were optimized in the gas-phase without symmetry constraints. The B3LYP level of theory with the 6-31G* basis set (B3LYP/6-31G* level) was employed for geometry optimizations, FMO calculations, frequency analyses and MEP calculations, except in the case of protonated CV ($CV^+$, see below). In calculations involving $TiO_2$, the LanL2DZ basis set was assigned to the titanium atoms [22]. TD-DFT calculations (UV-visible absorption spectrum simulations) were performed at the B3LYP/6-31+G* level of theory. Geometry optimization and simulation of the UV-visible absorption spectra of $CV^+$ were carried out using the B3LYP/6-31+G** and SVWN/6–31+G** levels of theory. For the MEP calculation, the van der Waals radius of the titanium atoms was specified as 2.2 Å [23,24]. The conductor-like polarized continuum model (CPCM) using ethanol (EtOH) was employed for all calculations determining the solvent effect, except the geometry optimizations.

## 3. Results and Discussion

### 3.1. Characteristics of CV

CV is a basic dye and coexists with counterions such as acetate and perchlorate. Hence, CV has multiple chemical structures. In this study, neutral CV (9-iminobenzo[a]phenoxazin-5-amine), its isomer (5-iminobenzo[a]phenoxazin-9-amine) and protonated CV are denoted as $CV_0$, $CV_{iso}$ and $CV^+$, respectively. The optimized structures of $CV_0$, $CV_{iso}$ and $CV^+$ in the gas phase are illustrated in Figure S2. For $CV^+$, structures with the positive charge at various locations ($NH_2^+$, $O^+$ and $N^+$) can be considered. However, these structures are not distinguished in the present work because this charge is delocalized over the entire molecule in DFT calculations [25]. Therefore, $CV^+$ was optimized as a structure with two amino groups and a positive charge distributed over the entire molecule.

Next, the UV-visible absorption spectra of CV in the gas phase were simulated (Figure 2A, black and red lines), as the photosensitizing dye's optical properties are among the most important factors in determining the photocatalytic activity of $TiO_2$-based photocatalysts and the PCEs of DSSCs [12]. The maximum absorption peaks ($\lambda_{max}$) of $CV_0$ and $CV_{iso}$ were observed at 491 and 432 nm, respectively (Table 1) [26]. In addition, the oscillator strengths ($f$) at $\lambda_{max}$ were calculated to be 0.513 and 0.5968, respectively. Good light-harvesting efficiency (LHE) is important for obtaining high photocurrent in $TiO_2$-based photocatalysts and DSSCs; this parameter can be calculated from the $f$ values using the following equation [10,11,27]:

$$LHE = 1 - 10^{-f} \tag{1}$$

The LHEs of $CV_0$ and $CV_{iso}$ were calculated to be 0.69 and 0.75, respectively, using Equation (1). It was expected that the solvent effect would result in a shift in the UV-visible absorption spectra and changes in the LHE values. The simulated UV-visible absorption spectra of $CV_0$ and $CV_{iso}$ using CPCM in EtOH showed a red-shift, and their LHE values increased (Figure 2A, blue and green lines). These results suggested that $CV_0$ and $CV_{iso}$ have excellent optical properties as photosensitizing dyes.

Like $CV_0$ and $CV_{iso}$, the UV-visible absorption spectrum of $CV^+$ was simulated using CPCM in EtOH (Figure 2B). The $\lambda_{max}$ of $CV^+$ was observed at 510 nm when the B3LYP/6-31+G** level of theory was used. High concentrations of $CV^+$ in aqueous solutions have been reported to exhibit a dimeric band at ~550 nm, which is attributed to H-aggregated species [28]. Additionally, the absorption peak of $CV^+$ on a Langmuir–Blodgett film is observed at ~525 nm [29]. On the other hand, the monomeric band of $CV^+$ is known to have a $\lambda_{max}$ of ~585 nm [25,28–30]. This band means that the energy of the charge–transfer state of $CV^+$ was overestimated in the TD-DFT calculation at the B3LYP/6-31+G** level of theory. Thus, other calculation methods were investigated, and the SVWN method was found to show relatively good agreement ($\lambda_{max}$ = 541 nm).
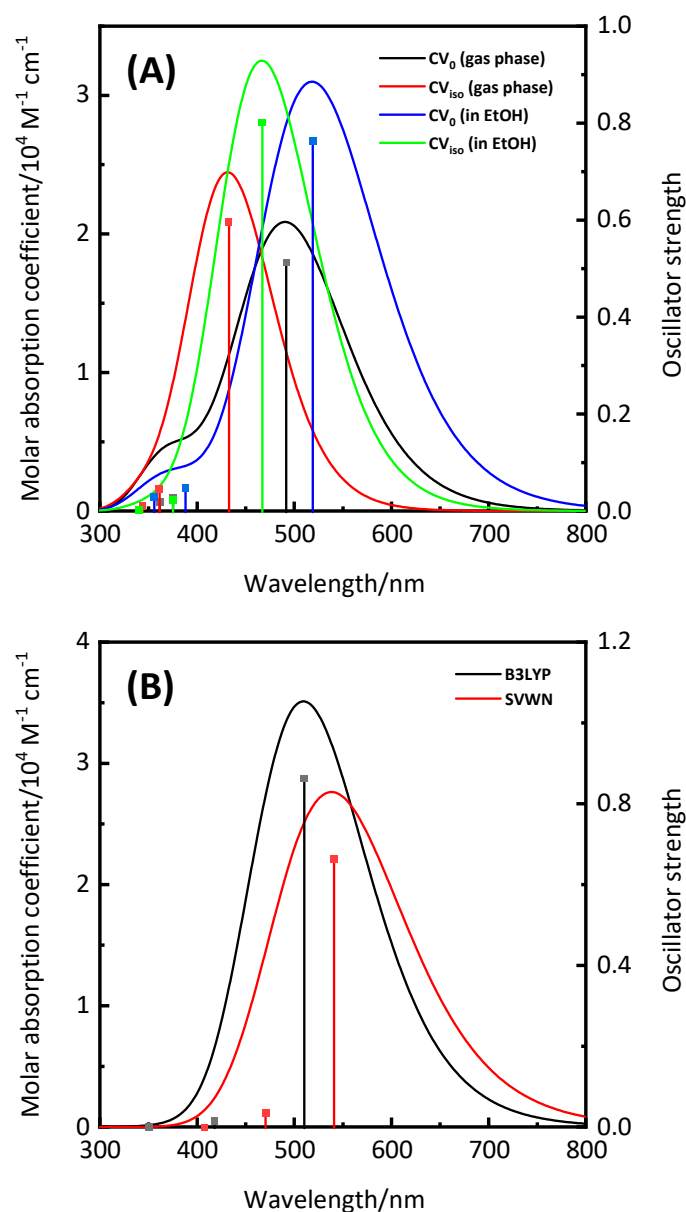
**Figure 2.** (**A**) Simulated UV-visible absorption spectra of $CV_0$ and $CV_{iso}$ in the gas phase and/or using CPCM in EtOH, calculated at the TD-B3LYP/6-31+G* level of theory; (**B**) simulated UV-visible absorption spectra of $CV^+$ using CPCM in EtOH, calculated at the TD-B3LYP/6-31+G** (black line) and TD-SVWN/6-31+G** (red line) levels of theory, respectively. Vertical lines indicate the calculated oscillator strengths.

In addition to the UV-visible absorption spectra, the highest occupied molecular orbital (HOMO) and lowest unoccupied molecular orbital (LUMO) levels of photosensitizing dyes play important roles in $TiO_2$-based photocatalysts and DSSCs [12]. Electron injection from the LUMO of the photoexcited dye to the CB of $TiO_2$ is the first process in $TiO_2$-based photocatalysis and DSSCs. The HOMO level is related to the reduction of the oxidized dye formed by electron injection. Therefore, FMO calculations of CV using CPCM in EtOH were performed. The FMOs and energy diagrams of CV are shown in Figures S3 and S4.

**Table 1.** Calculated maximum absorption peaks ($\lambda_{max}$), molar absorption coefficients ($\varepsilon$), energies of singlet excited states ($E_{S1}$), oscillator strengths ($f$) and light-harvesting efficiencies (LHE) of $CV_0$, $CV_{iso}$ and $CV^+$.

| Dyes | Conditions | $\lambda_{max}$ (nm) | $\varepsilon$ ($10^4$ M$^{-1}$ cm$^{-1}$) | $E_{S1}$ (eV) | $f$ | LHE |
|---|---|---|---|---|---|---|
| $CV_0$ | gas phase | 491 | 2.09 | 2.52 | 0.513 | 0.69 |
| | in EtOH | 518 | 3.10 | 2.39 | 0.7643 | 0.83 |
| $CV_{iso}$ | gas phase | 432 | 2.44 | 2.87 | 0.5968 | 0.75 |
| | in EtOH | 467 | 3.25 | 2.66 | 0.8008 | 0.84 |
| $CV^+$ | in EtOH | 510 | 3.51 | 2.43 | 0.8641 | 0.86 |
| $CV^{+\,a}$ | in EtOH | 541 | 2.76 | 2.29 | 0.6637 | 0.78 |

a: calculation method was using SVWN/6-31+G** level.

According to the TD-DFT calculations, the UV-visible absorption spectra of CV are dominated by the transition from the ground state to the singlet excited state attributed to the HOMO–LUMO transition. The HOMO and LUMO of CV are distributed over the whole molecule due to its extended $\pi$-conjugation. In the cases of $CV_0$ and $CV_{iso}$, the LUMOs, in particular, are delocalized around the aromatic rings with the imino moiety. This result suggests electron transfer from the aromatic ring with the amino group to the region near the imino moiety, i.e., the amino group acts as a donor. The LUMO levels of $CV_0$ and $CV_{iso}$ were calculated to be −2.55 eV and −2.42 eV, respectively. These values are much higher than the CB level of $TiO_2$ (−4.0 eV) [10–12,27], which indicates the possibility of electron injection from the LUMO of $CV_0$ and/or $CV_{iso}$ to the CB of $TiO_2$. Additionally, the HOMO levels of $CV_0$ and $CV_{iso}$ were calculated to be −5.14 eV and −5.33 eV, respectively. These values are lower than the redox potential of the iodide ion/triiodide ion ($I^-/I_3^-$, −4.8 eV), which is a common redox couple in the electrolyte solution in DSSCs [10–12,27]. This result indicates that the oxidized $CV_0$ and $CV_{iso}$ formed by electron injection can be regenerated in the electrolyte. In conclusion, CV was confirmed to act as a photosensitizing dye in $TiO_2$-based photocatalysts and DSSCs.

The $CV^+$ results calculated at the B3LYP/6-31+G** level (HOMO and LUMO levels of −6.23 eV and −3.67 eV, respectively) suggested the possibility of electron injection and regeneration in the electrolyte. However, the LUMO level calculated at the SVWN/6-31+G** level of theory was lower than the CB level of $TiO_2$. These results suggested that the accuracy of both the optical properties and FMO levels of $CV^+$ could not be guaranteed. Therefore, $CV^+$ was excluded from further study, and only the details of $CV_0$ and $CV_{iso}$ were investigated.

*3.2. Geometry Structures and Characteristics of CV–OTES–C2*

Subsequently, geometry optimization of $CV_0$ and/or $CV_{iso}$ attached to OTES–C2 in the gas phase was performed (Figure 3). These dyes are denoted as $CV_0$–OTES–C2 and $CV_{iso}$–OTES–C2, respectively. Here, it must be assumed that the alkyl alkoxysilane moieties exist in multiple conformations due to C–C bond rotation of the alkyl chain. In this study, the straight alkyl chain configuration was chosen as the starting geometry because the SCAs form a SAMs, attributed to the formation of the siloxane network [13,14].

The hydroxyl group and secondary amine moieties on the alkyl chain resulted from the epoxy-ring-opening reaction between $CV_0$ and/or $CV_{iso}$ and OTES–C2. An apparent CH–O interaction between the hydroxyl group of the alkyl chain and the hydrogen atom of the aromatic ring of $CV_0$ and/or $CV_{iso}$ can be observed in $CV_0$–OTES–C2 and $CV_{iso}$–OTES–C2. The calculated distances between the oxygen and hydrogen atoms were in the range 2.35–2.39 Å, which is shorter than the sum of the van der Waals radii of the oxygen and hydrogen atoms (2.72 Å) [31]. This result further supported the occurrence of the CH–O interaction.
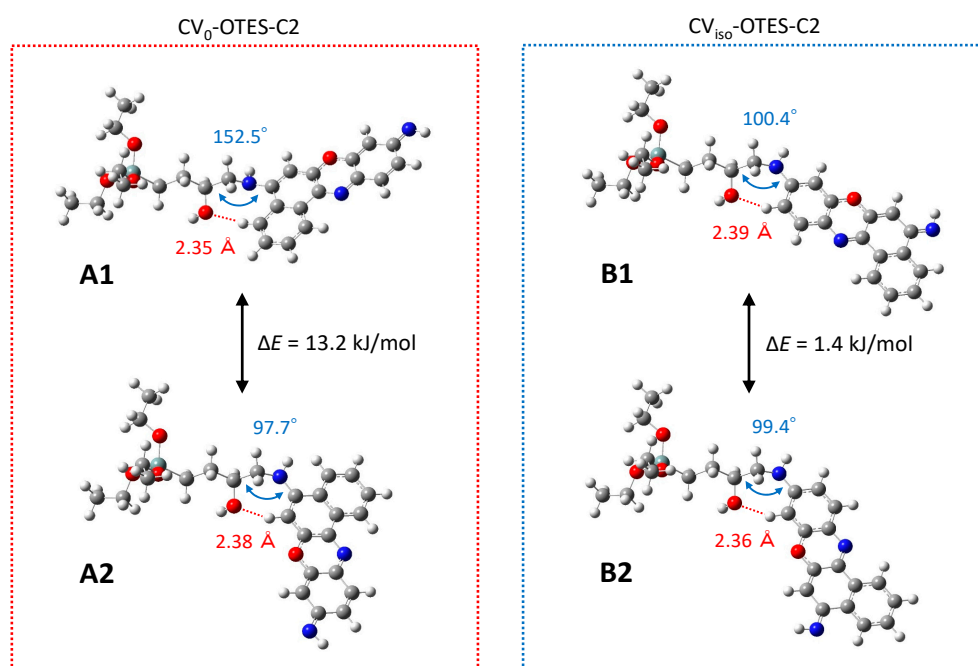
**Figure 3.** Optimized structures of $CV_0$–OTES–C2 and $CV_{iso}$–OTES–C2 in the gas phase, calculated at the B3LYP/6-31G* level of theory. The geometries of $CV_0$–OTES–C2 and $CV_{iso}$–OTES–C2 are labeled as A1 and A2 and B1 and B2, respectively. The distance of the CH–O interaction, C–C–N–C dihedral angle and energy difference ($\Delta E$) are shown in red, blue and black, respectively (see the text for further details).

The CH–O interaction was expected to affect the geometry of CV–OTES–C2. In particular, a dihedral angle distortion was expected due to the steric hindrance of the condensed aromatic ring. To confirm this, geometry optimizations of $CV_0$–OTES–C2 and $CV_{iso}$–OTES–C2 were performed with different torsional angles for the secondary amine moieties and the dihedral angles of the secondary amine moieties (C–C–N–C dihedral angle, see Figure 3) were examined. The optimized structures of $CV_0$–OTES–C2 and $CV_{iso}$–OTES–C2 were labeled as A1/A2 and B1/B2, respectively. As expected, the C–C–N–C dihedral angle of $CV_0$–OTES–C2 (conformation A1) was 152.5°, which represented a remarkable distortion compared to that in the other conformations. Since this distortion of the dihedral angle may result in energy differences (sum of electronic and thermal energy; $\Delta E$) between the different geometries, frequency analysis was then performed. The $\Delta E$ between the different optimized geometries of $CV_0$–OTES–C2 (conformations A1 and A2) was 13.2 kJ/mol, with a bias toward A2. On the other hand, the two conformations of $CV_{iso}$–OTES–C2 (conformation B1 and B2) were competitive, as $\Delta E$ was 1.4 kJ/mol. The $\Delta E$ between the conformations of CV–OTES–C2 was clearly due to the condensed aromatic rings of CV and the CH–O interaction. Based on the above results, it was concluded that the CH–O interaction influences the conformation of CV–OTES–C2.

Figure 4 and Table 2 show the simulated UV-visible absorption spectra and calculated optical properties of $CV_0$–OTES–C2 and $CV_{iso}$–OTES–C2 using CPCM in EtOH. The $\lambda_{max}$ of CV–OTES–C2 was red-shifted by 12–22 nm compared with that of isolated CV. Additionally, the LHE increased slightly. These results indicated that CV–OTES–C2 was more promising as a photosensitizing dye than isolated CV.
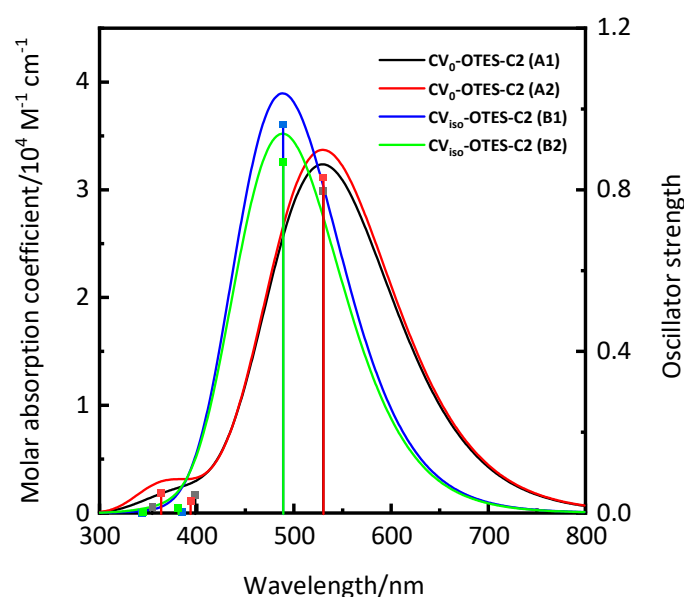
**Figure 4.** Simulated UV-visible absorption spectra of $CV_0$–OTES–C2 and $CV_{iso}$–OTES–C2 using conductor-like polarized continuum model (CPCM) in ethanol (EtOH). Calculations were carried out at the TD-B3LYP/6-31+G* level of theory. Vertical lines indicate the calculated oscillator strengths.

**Table 2.** Calculated maximum absorption peaks ($\lambda_{max}$), molar absorption coefficients ($\varepsilon$), energies of singlet excited states ($E_{S1}$), oscillator strengths ($f$) and light-harvesting efficiencies (LHE) of $CV_0$–OTES–C2 and $CV_{iso}$–OTES–C2.

| Dyes | $\lambda_{max}$ (nm) | $\varepsilon$ ($10^4$ $M^{-1}$ $cm^{-1}$) | $E_{S1}$ (eV) | $f$ | LHE |
|---|---|---|---|---|---|
| $CV_0$–OTES–C2 (A1) | 530 | 3.24 | 2.34 | 0.7979 | 0.84 |
| $CV_0$–OTES–C2 (A2) | 530 | 3.37 | 2.34 | 0.8317 | 0.85 |
| $CV_{iso}$–OTES–C2 (B1) | 488 | 3.89 | 2.53 | 0.9614 | 0.89 |
| $CV_{iso}$–OTES–C2 (B2) | 489 | 3.52 | 2.54 | 0.8688 | 0.86 |

FMO calculations of CV–OTES–C2 (Figure 5) were performed, and energy diagrams were constructed (Figure 6). The HOMOs of CV–OTES–C2 are distributed even near the secondary amine moieties; the red-shift of $\lambda_{max}$ was attributed to this result. The LUMOs of CV–OTES–C2 are delocalized around the aromatic ring with the imino moiety, similar to isolated CV. The LUMO levels of CV–OTES–C2 were in the range of −2.36 eV to −2.61 eV, which are higher than the CB level of TiO$_2$ (−4.0 eV). Additionally, the calculated HOMO levels (−4.99 eV to −5.17 eV) of CV–OTES–C2 are lower than the redox potential of $I^-/I_3^-$ (−4.8 eV) in an electrolyte solution. These results confirm that CV–OTES–C2 could act as a photosensitizing dye in TiO$_2$-based photocatalysts and DSSCs. However, the distribution of the LUMOs around the aromatic ring with the imino moiety may be unfavorable in terms of electron injection, because the LUMOs are located relatively distant from the TiO$_2$ surface.
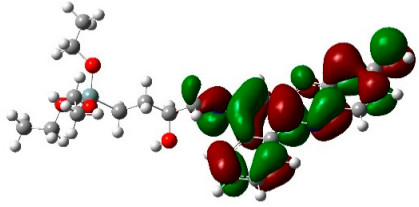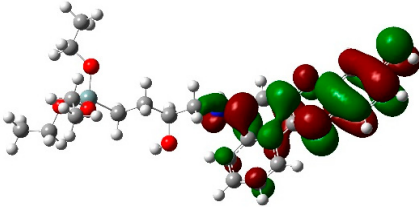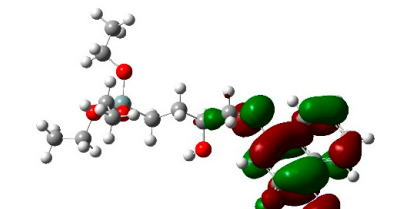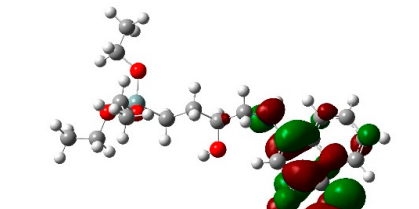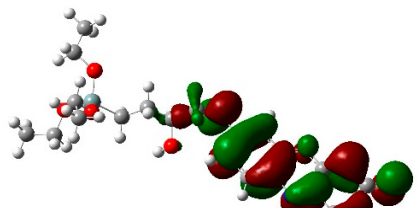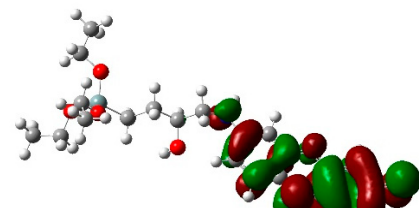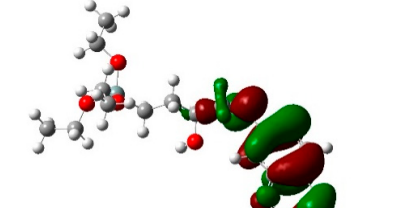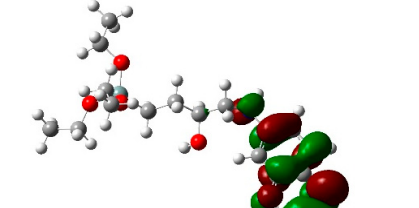
| | HOMO | LUMO |
|---|---|---|
| CV$_0$-OTES-C2 (A1) |  -5.17 eV |  -2.61 eV |
| CV$_0$-OTES-C2 (A2) |  -4.99 eV |  -2.47 eV |
| CV$_{iso}$-OTES-C2 (B1) |  -5.17 eV |  -2.37 eV |
| CV$_{iso}$-OTES-C2 (B2) |  -5.16 eV |  -2.36 eV |

**Figure 5.** Highest occupied molecular orbitals (HOMO) and lowest unoccupied molecular orbitals (LUMOs) of CV$_0$–OTES–C2 and CV$_{iso}$–OTES–C2 using CPCM in EtOH. Calculations were carried out at the B3LYP/6-31G* level of theory. Surface isovalue: 0.02 e/bohr$^3$.
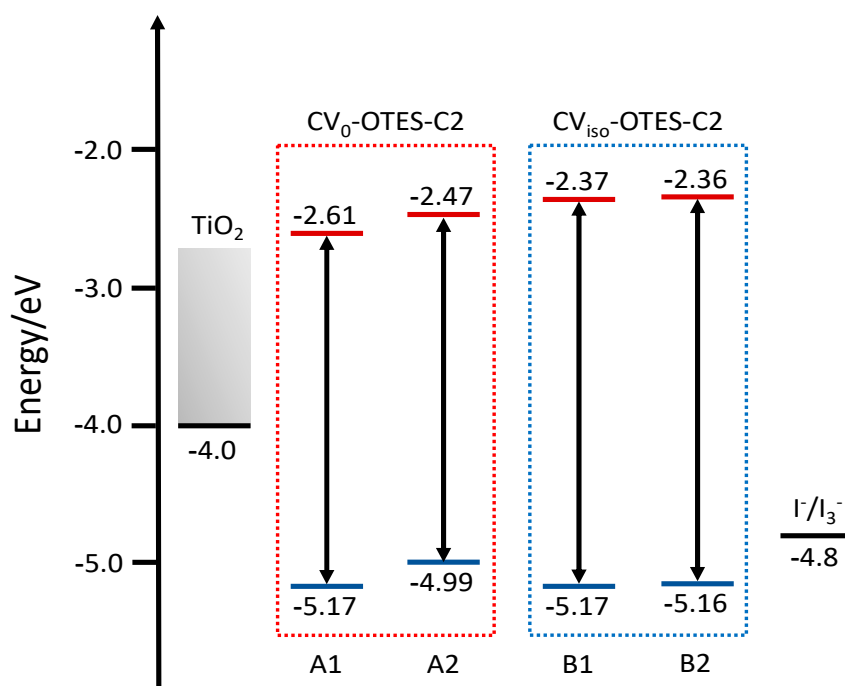
**Figure 6.** Calculated energy levels of the HOMOs (blue lines) and LUMOs (red lines) for $CV_0$–OTES–C2 and $CV_{iso}$–OTES–C2 using CPCM in EtOH.

### 3.3. Effect of the Alkyl Chain Length of OTES–Cn

To determine the effect of the alkyl chain length of OTES–Cn, the UV-visible absorption spectra and FMOs of $CV_0$–OTES–C4, $CV_0$–OTES–C8, $CV_{iso}$–OTES–C4 and $CV_{iso}$–OTES–C8 were investigated. The geometries of these molecules are illustrated in Figure S5. According to frequency analysis, the bent molecular configuration (A2) was dominant for $CV_0$–OTES–C2; however, $CV_0$–OTES–C2 adsorbed on the $TiO_2$ surface may adopt the unbent molecular configuration (A1) due to the large steric hindrance between adjacent CV moieties and/or between the SAM surface and CV moieties (see below for further details). Therefore, the details of the unbent molecular configurations of $CV_0$–OTES–Cn and $CV_{iso}$–OTES–Cn (A1 and B1) were investigated. The simulated UV-visible absorption spectra of the dyes did not exhibit significant differences. The alkyl chain length of OTES–Cn did not affect the optical properties of CV–OTES–Cn (Figure S6). It should be noted that the gas-phase spectra were compared because the TD-DFT calculation for CV–OTES–C8 using CPCM in EtOH was very expensive. As would be expected from this result, the distributions of the FMOs and the energy levels of the HOMOs and LUMOs of CV–OTES–Cn were also in good agreement (Figures S7 and S8). Consequently, the alkyl chain length of OTES–Cn was not confirmed to significantly affect the UV-visible absorption spectra and FMOs of CV–OTES–Cn. In other words, if the photocurrent of actual $TiO_2$-based photocatalysts and DSSCs is enhanced by the alkyl chain length of OTES–Cn, it may be due to the controlled molecular orientation of CV due to the formation of the SAMs.

### 3.4. Configuration of CV–OTES–C2 Adsorbed on a $TiO_2$ Cluster

To understand the structure of CV–OTES–C2 adsorbed on the $TiO_2$ surface, geometry optimization of a $TiO_2$ cluster and $CV_0$–OTES–C2 or $CV_{iso}$–OTES–C2 adsorbed on the $TiO_2$ cluster were performed. For the geometry optimization of the $TiO_2$ cluster, the anatase $TiO_2$ (101) surface model was selected because anatase is known to exhibit higher photocatalytic activity than rutile and the (101) surface has the lowest surface energy [32]. A cluster size of $Ti_6O_{15}H_6$ was employed, and the cluster optimized at the B3LYP/6-31G*/LanL2DZ level of theory to compromise between computational costs and accuracy (Figure S9).

Figure 7 illustrates CV–OTES–C2 adsorbed conformations on the TiO$_2$ cluster (tridentate bridging model, calculated in the gas phase). The calculated bond lengths between the alkoxysilane oxygen atoms and connected titanium atoms were ~1.86 Å, comparable to the Ti–O bond lengths in the Ti$_6$O$_{15}$H$_6$ cluster (1.80–1.84 Å). These bond lengths indicated strong chemical adsorption of CV–OTES–C2 onto the TiO$_2$ (101) surface.
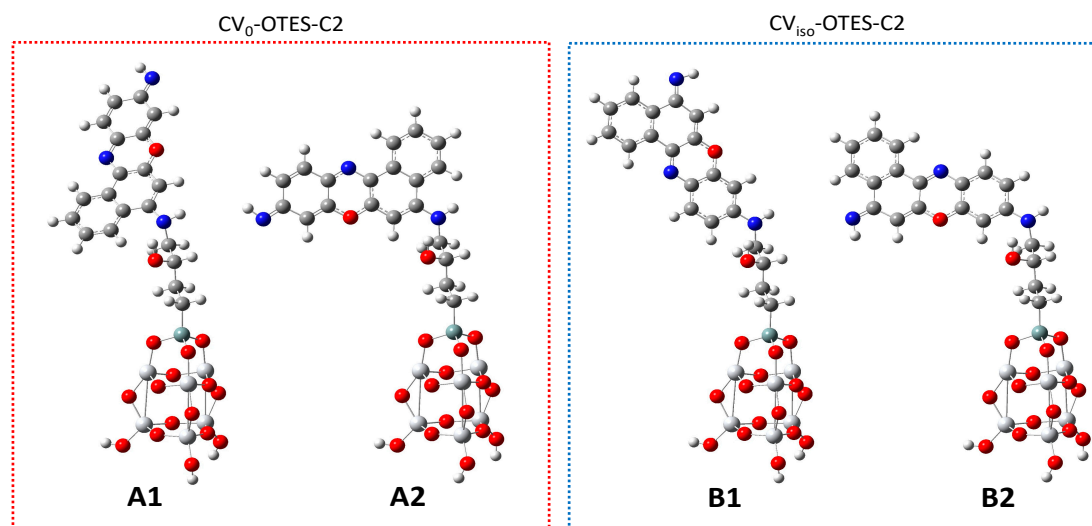


**Figure 7.** Optimized structures of CV–OTES–C2 adsorbed on the TiO$_2$ cluster in the gas phase, calculated using the B3LYP/6-31G*/LanL2DZ level of theory. The conformations of CV$_0$–OTES–C2 and CV$_{iso}$–OTES–C2 are labeled as A1 and A2 and B1 and B2, respectively.

The molecular length provided information related to the conformation of CV–OTES–C2 adsorbed on the TiO$_2$ surface. The long axes (distance between the silane atom on the alkoxysilane moiety and the nitrogen atom on the imino moiety) of CV$_0$–OTES–C2 and CV$_{iso}$–OTES–C2 in the unbent conformations (A1 and B1) were 15.9 Å (Figure S10). In comparison, those of the bent conformations (A2 and B2) were 12.1 Å and 12.3 Å, respectively, and had shorter contact distances between the CV moiety and the TiO$_2$ surface compared to geometries A1 and B1. Additionally, the short axes (the distance between the nitrogen atoms on the imino moieties and those on the secondary amine moieties) of the bent conformations were 9.5 Å and 9.6 Å, respectively. If a SAMs based on OTES–Cn was present on the TiO$_2$ surface, the bent molecular geometry would be unlikely due to the steric hindrance between adjacent CV moieties and/or between the SAMs surface and CV moieties. Therefore, it was expected that the unbent conformation of CV–OTES–C2 would predominate on the TiO$_2$ surface.

*3.5. FMO, DOS Spectra and MEP of CV–OTES–C2 Adsorbed on the TiO$_2$ Cluster*

Subsequently, the FMOs and DOS spectra of CV–OTES–C2 in the unbent conformations (A1 and B1) adsorbed on the TiO$_2$ cluster were calculated to investigate the electron injection from CV–OTES–C2 to TiO$_2$ (Figures 8 and 9). As in the case of isolated CV–OTES–C2, the HOMOs of CV–OTES–C2 adsorbed on the TiO$_2$ cluster were distributed around the CV and secondary amine moieties. At the same time, the LUMOs were located around the titanium atoms connected to the alkoxysilane oxygens. This result indicates that electron injection would occur from CV–OTES–C2 to TiO$_2$. However, it should be noted that the CB level of Ti$_6$O$_{15}$H$_4$ was estimated to be −2.72 eV by the FMO calculation using CPCM in EtOH.

CV$_0$-OTES-C2

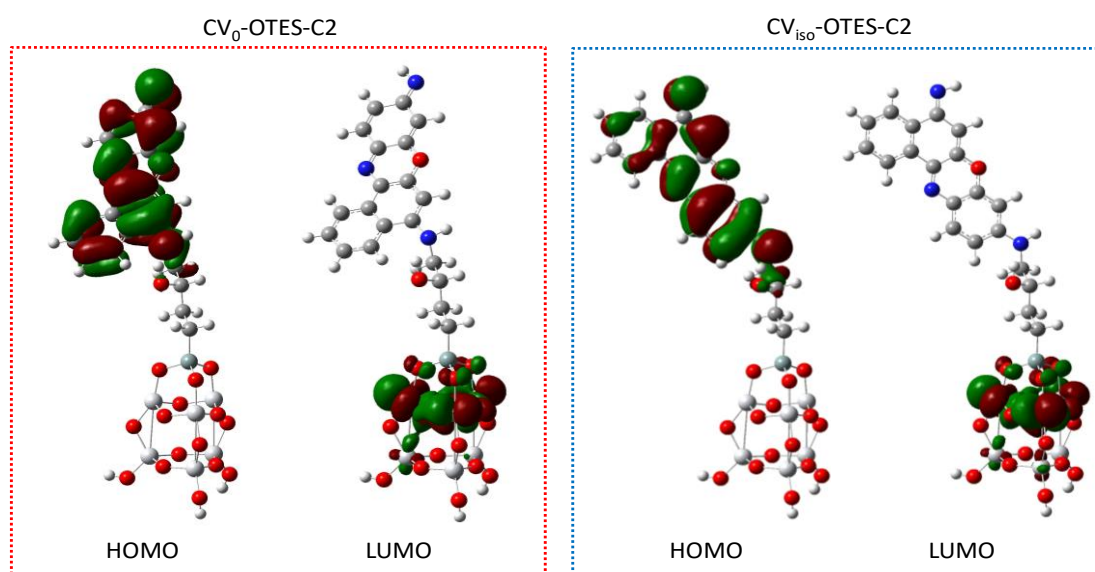CV$_{iso}$-OTES-C2

HOMO  LUMO  HOMO  LUMO

**Figure 8.** HOMOs and LUMOs of CV$_0$–OTES–C2 or CV$_{iso}$–OTES–C2 adsorbed on the TiO$_2$ cluster using CPCM in EtOH, calculated at the B3LYP/6-31G*/LanL2DZ level of theory. Surface isovalue: 0.02 e/bohr$^3$.
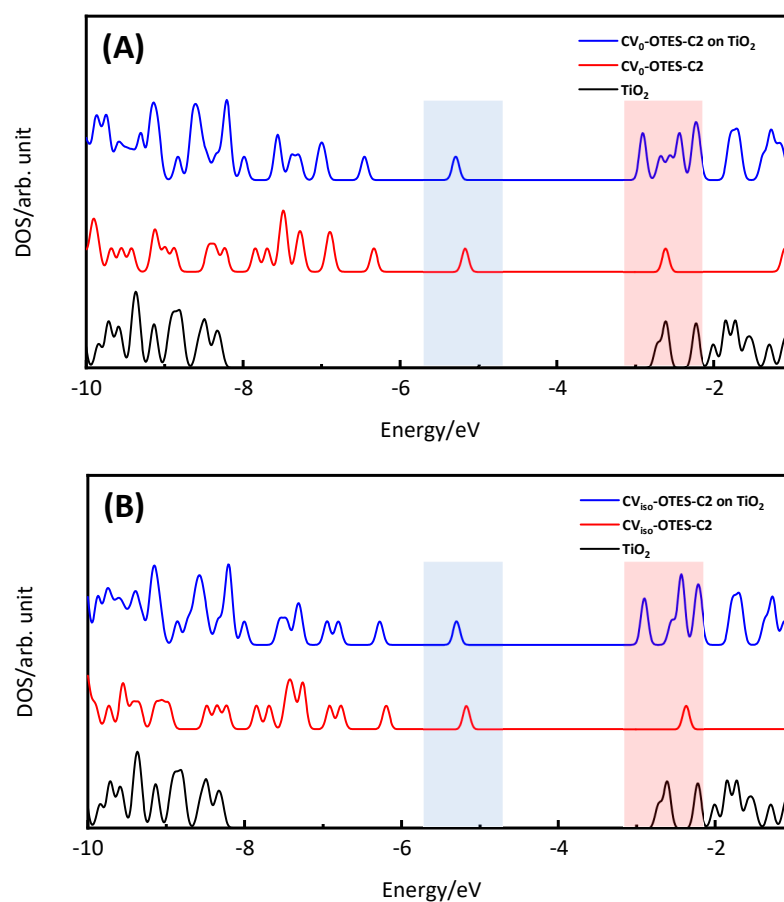
**(A)**

- CV$_0$-OTES-C2 on TiO$_2$
- CV$_0$-OTES-C2
- TiO$_2$

DOS/arb. unit

Energy/eV

**(B)**

- CV$_{iso}$-OTES-C2 on TiO$_2$
- CV$_{iso}$-OTES-C2
- TiO$_2$

DOS/arb. unit

Energy/eV

**Figure 9.** Density of state (DOS) spectra of (**A**) CV$_0$–OTES–C2 and (**B**) CV$_{iso}$–OTES–C2 adsorbed on the TiO$_2$ cluster using CPCM in EtOH. Black, red and blue lines correspond to the TiO$_2$ cluster, isolated CV–OTES–C2 and CV–OTES–C2 adsorbed on the TiO$_2$ cluster. Blue and red bars indicate the HOMO and LUMO.

According to the DOS spectra, the HOMO and LUMO levels of CV–OTES–C2 were downshifted by adsorption onto TiO$_2$. In particular, the downshift of the LUMO level was remarkable and suggested degeneracy between the CB level of TiO$_2$ and the LUMO level of CV–OTES–C2. This bandgap reduction may induce efficient visible light absorption and electron injection.

The MEPs of isolated CV–OTES–C2 and CV–OTES–C2 adsorbed on the TiO$_2$ cluster were calculated to complement the FMO calculations and DOS spectra (Figure 10). The MEP identifies the nucleophilic reaction sites and electrophilic reaction sites [27]. In all dyes, the imino moiety exhibited the highest nucleophilic potential. In isolated CV–OTES–C2, the hydrogen atom of the hydroxyl group and the secondary amine moiety on the alkyl chain exhibited electrophilic potentials. On the other hand, for CV–OTES–C2 to be adsorbed on the TiO$_2$ cluster, the titanium atoms connected to the alkoxysilane oxygens needed to have the greatest electrophilic potential. This indicates that the electron injection to TiO$_2$ occurs via the alkoxysilane moiety, i.e., these results support those of the FMO calculations and DOS spectra.
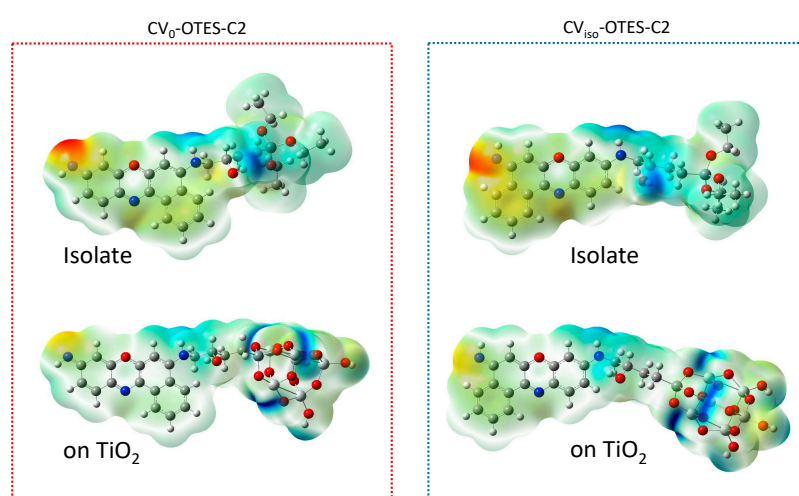


**Figure 10.** Molecular electrostatic potential (MEP) of isolated CV–OTES–C2 and CV$_{iso}$–OTES–C2 adsorbed on the TiO$_2$ cluster using CPCM in EtOH. Red and blue indicate electron-rich (negative charge) and electron-deficient regions (positive charge), respectively; the electrostatic potential increases in the order red < orange < yellow < green < cyan < blue. Color code of the MEP maps of the isolated CV–OTES–C2 and the CV–OTES–C2 adsorbed on the TiO$_2$ cluster ranged from −0.078 a.u. to 0.078 a.u. and from −0.11 a.u. to 0.11 a.u., respectively.

### 3.6. Simulated Short-Circuit Current Density

The PCE of DSSC is calculated using the following equation [10,27]:

$$\text{PCE} = (J_{sc} \times V_{oc} \times \text{FF})/I_0 \tag{2}$$

Here, $J_{sc}$, $V_{oc}$, FF and $I_0$ are the short-circuit current density, open-circuit voltage, fill factor and incident light flux, respectively. $J_{sc}$ and $V_{oc}$ are important factors in the enhancement of the PCE. $J_{sc}$ is defined by the following equation [10,11,27]:

$$J_{sc} = \int (\text{LHE}(\lambda) \times \Phi_{inject} \times \eta_{collect}) \, d\lambda \tag{3}$$

where LHE($\lambda$), $\Phi_{inject}$ and $\eta_{collect}$ are the LHE at a given wavelength, the electron injection efficiency and the charge collection efficiency, respectively. It was assumed that all the components of the DSSC were constant except for the photosensitizing dye. Hence, $\eta_{collect}$ can be assumed to be constant.

$\Phi_{\text{inject}}$ is related to the injection driving force ($\Delta G_{\text{inject}}$) of the electrons injected from the excited dyes to the TiO$_2$. $\Delta G_{\text{inject}}$ can be estimated using the following equation [10,11,27]:

$$\Delta G_{\text{inject}} = E^{\text{dye}*} - E_{\text{CB}} = (E^{\text{dye}} - E_{\text{S1}}) - E_{\text{CB}} \tag{4}$$

$E^{\text{dye}*}$, $E^{\text{dye}}$, $E_{\text{CB}}$ and $E_{\text{S1}}$ are the oxidation potential of the photosensitizing dye in the excited state, the redox potential of the photosensitizing dye in the ground state, the reduction potential of the CB level of TiO$_2$ (4.0 eV) and the energy of the singlet excited state. $E^{\text{dye}}$ can be estimated as the negative of the HOMO level [11]. $E_{\text{S1}}$ is the vertical transition energy associated with the $\lambda_{\text{max}}$ value obtained from the UV-visible absorption spectra and is listed in Tables 1 and 2. The $E^{\text{dye}}$, $E^{\text{dye}*}$ and $\Delta G_{\text{inject}}$ values of isolated CV–OTES–C2 are listed in Table 3.

**Table 3.** Redox potential in the ground state ($E^{\text{dye}}$), oxidation potential in the excited state ($E^{\text{dye}*}$) and injection driving force ($\Delta G_{\text{inject}}$) of isolated CV–OTES–C2.

| Dyes | $E^{\text{dye}}$ (eV) | $E^{\text{dye}*}$ (eV) | $\Delta G_{\text{inject}}$ (eV) |
|---|---|---|---|
| CV$_0$–OTES–C2 (A1) | 5.17 | 2.83 | −1.17 |
| CV$_0$–OTES–C2 (A2) | 4.99 | 2.65 | −1.35 |
| CV$_{\text{iso}}$–OTES–C2 (B1) | 5.17 | 2.64 | −1.36 |
| CV$_{\text{iso}}$–OTES–C2 (B2) | 5.16 | 2.62 | −1.38 |

The $\Delta G_{\text{inject}}$ values for the A1, A2, B1 and B2 conformations were −1.17 eV, −1.35 eV, −1.36 eV and −1.38 eV; these values were more negative than that of $E_{\text{CB}}$. This result indicates that the excited state of CV–OTES–C2 lies above the CB edge of TiO$_2$, i.e., that electron injection should occur from the excited CV–OTES–C2 to the CB of TiO$_2$.

The $\Delta G_{\text{inject}}$ of CV$_0$–OTES–C2 (A1) is the lowest, suggesting that conformation A1 would exhibit slower electron injection and a lower $J_{\text{SC}}$ than the other geometries. However, the bent molecular conformations of CV–OTES–C2 (A2 and B2) may not form on the TiO$_2$ surface (see above for further details). The UV-visible absorption spectrum of conformation A1 also has a broader absorption band than geometry B1 (Figure 4). The LHE depends not only on absorbance but also on the width and tails of the absorption band. Photosensitizing dyes with wider absorption bands in the visible/IR region can achieve much higher LHEs [11]. Therefore, it is expected that the characteristics of CV$_0$–OTES–C2 (A1) would contribute significantly to enhancing the photocurrent in TiO$_2$-based photocatalysts and DSSCs.

## 4. Conclusions

This article reported a DFT and TD-DFT study of CV–OTES–Cn to determine the influence of OTES–Cn on photosensitizing dyes' geometry. The potential of CV–OTES–Cn to act as a photosensitizing dye was also evaluated. The hydroxyl group formed by the epoxy-opening reaction resulted in a CH–O interaction between CV and the covalently attached OTES–Cn. This CH–O interaction significantly influenced the conformation of CV–OTES–Cn and distorted the C–C–N–C dihedral angle due to the steric hindrance of the condensed aromatic ring of CV. According to TD-DFT calculations (simulated UV-visible absorption spectra), CV–OTES–Cn has excellent optical properties and should act as a promising photosensitizer for TiO$_2$-based photocatalysts and DSSCs. Additionally, the results of FMO calculations, DOS spectra and MEP calculations indicated that electron injection proceeds from CV–OTES–Cn to TiO$_2$. In particular, the characteristics of the unbent molecular geometry of CV–OTES–Cn (conformation A1) should contribute significantly to enhancing photocurrent in TiO$_2$-based photocatalysts and DSSCs. Overall, the following conclusions were drawn: (i) SAMs based on the OTES–Cn on the TiO$_2$ surface can control CV conformation covalently attached to the terminal functional group of OTES–Cn (CV–OTES–Cn); (ii) CV–OTES–Cn has potential as a promising photosensitizer for TiO$_2$-based photocatalysts and DSSCs. This article's findings should enhance covalent attachment strategies between photosensitizing dyes and TiO$_2$ and improve TiO$_2$-based photocatalysts and DSSCs.

## References

1.　Lu, G.; Liu, X.; Zhao, L.; Zhang, P.; Gao, Y. Synergistic photocatalytic performance of chemically modified amino phthalocyanine-GPTMS/$TiO_2$ for the degradation of Acid Black 1. *Inorg. Chem. Commun.* **2020**, *113*, 107795. [CrossRef]

2.　Kakiage, K.; Aoyama, Y.; Yano, T.; Oya, K.; Fujisawa, J.-I.; Hanaya, M. Highly-efficient dye-sensitized solar cells with collaborative sensitization by silyl-anchor and carboxy-anchor dyes. *Chem. Commun.* **2015**, *51*, 15894–15897. [CrossRef] [PubMed]

3.　Bhat, V.T.; Duspara, P.A.; Seo, S.; Abu Bakar, N.S.B.; Greaney, M.F. Visible light promoted thiol-ene reactions using titanium dioxide. *Chem. Commun.* **2015**, *51*, 4383–4385. [CrossRef] [PubMed]

4.　Rodriguez-Gonzalez, V.; Obregon, S.; Patron-Soberano, O.A.; Terashima, C.; Fujishima, A. An approach to the photocatalytic mechanism in the $TiO_2$-nanomaterials microorganism interface for the control of infectious processes. *Appl. Catal. B Environ.* **2020**, *270*, 118853. [CrossRef]

5.　Paszkiewicz-Gawron, M.; Makurat, S.; Rak, J.; Zdrowowicz, M.; Lisowski, W.; Zaleska-Medynska, A.; Kowalska, E.; Mazierski, P.; Luczak, J. Theoretical and experimental studies on the visible light activity of $TiO_2$ modified with halide-based ionic liquids. *Catalysts* **2020**, *10*, 371. [CrossRef]

6.　Rahimi, R.; Moghaddas, M.M.; Zargari, S. Investigation of the anchoring silane coupling reagent effect in porphyrin sensitized mesoporous V-$TiO_2$ on the photodegradation efficiency of methyl orange under visible light irradiation. *J. Sol-Gel Sci. Technol.* **2013**, *65*, 420–429. [CrossRef]

7.　Sil, M.C.; Kavungathodi, M.F.M.; Nithyanandhan, J. Effect and position of spiro-bipropylenedioxythiophene π-spacer in donor-π-spacer-acceptor dyes for dye-sensitized solar cell. *Dyes Pigment.* **2019**, *161*, 313–323. [CrossRef]

8.　Zhu, H.-C.; Zhang, J.; Wang, Y.-L. Adsorption orientation effects of porphyrin dyes on the performance of DSSC: Comparison of benzoic acid and tropolone anchoring groups binding onto the $TiO_2$ anatase (101) surface. *Appl. Surf. Sci.* **2018**, *433*, 1137–1147. [CrossRef]

9.　Ooyama, Y.; Shimada, Y.; Inoue, S.; Nagano, T.; Fujikawa, Y.; Komaguchi, K.; Imae, I.; Harima, Y. New molecular design of donor-π-acceptor dyes for dye-sensitized solar cells: Control of molecular orientation and arrangement on $TiO_2$ surface. *New J. Chem.* **2011**, *35*, 111–118. [CrossRef]

10.　Yang, Z.; Liu, C.; Shao, C.; Lin, C.; Liu, Y. First-Principles Screening and Design of Novel Triphenylamine-Based D-π-A Organic Dyes for Highly Efficient Dye-Sensitized Solar Cells. *J. Phys. Chem. C* **2015**, *119*, 21852–21859. [CrossRef]

11.　Ud-Din Khan, S.; Mahmood, A.; Rana, U.A.; Haider, S. Utilization of electron-deficient thiadiazole derivatives as π-spacer for the red shifting of absorption maxima of diarylamine-fluorene based dyes. *Theor. Chem. Acc.* **2015**, *134*, 1–7. [CrossRef]

12. Li, P.; Wang, Z.; Zhang, H. Rigidified and expanded N-annulated perylenes as efficient donors in organic sensitizers for application in solar cells. *Phys. Chem. Chem. Phys.* **2019**, *21*, 10488–10496. [CrossRef] [PubMed]

13. Zhan, F.; Xiong, L.; Liu, F.; Li, C. Grafting hyperbranched polymers onto $TiO_2$ nanoparticles via thiol-yne click chemistry and its effect on the mechanical, thermal and surface properties of polyurethane coating. *Materials* **2019**, *12*, 2817. [CrossRef] [PubMed]

14. Meroni, D.; Lo Presti, L.; Di Liberto, G.; Ceotto, M.; Acres, R.G.; Prince, K.C.; Bellani, R.; Soliveri, G.; Ardizzone, S. A Close Look at the Structure of the $TiO_2$-APTES Interface in Hybrid Nanomaterials and Its Degradation Pathway: An Experimental and Theoretical Study. *J. Phys. Chem. C* **2017**, *121*, 430–440. [CrossRef] [PubMed]

15. Krishnakumar, B.; Balakrishna, A.; Arranja, C.T.; Dias, C.M.F.; Sobral, A.J. Chemically modified amino porphyrin/$TiO_2$ for the degradation of Acid Black 1 under day light illumination. *Spectrochim. Acta Part A Mol. Biomol. Spectrosc.* **2017**, *176*, 134–141. [CrossRef]

16. Luitel, T.; Zamborini, F.P. Covalent Modification of Photoanodes for Stable Dye-Sensitized Solar Cells. *Langmuir* **2013**, *29*, 13582–13594. [CrossRef]

17. Pandit, B.; Luitel, T.; Cummins, D.R.; Thapa, A.K.; Druffel, T.; Zamborini, F.; Liu, J. Spectroscopic Investigation of Photoinduced Charge-Transfer Processes in FTO/$TiO_2$/N719 Photoanodes with and without Covalent Attachment through Silane-Based Linkers. *J. Phys. Chem. A* **2013**, *117*, 13513–13523. [CrossRef]

18. Abdulelah, H.; Ali, B.; Mahdi, M.A.; Abdullah, A.Q.; Hassan, J.J.; Al-Taay, H.F.; Jennings, P. Fabrication and characterization of porous CdS/dye sensitized solar cells. *J. Sol. Energy* **2016**. [CrossRef]

19. Tan, H.; Pan, C.; Wang, G.; Wu, Y.; Zhang, Y.; Yu, G.; Zhang, M. A comparative study on properties of two phenoxazine-based dyes for dye-sensitized solar cells. *Dye. Pigment.* **2014**, *101*, 67–73. [CrossRef]

20. Hong, Y.; Iqbal, Z.; Yin, X.; Cao, D. Synthesis of double D-A branched organic dyes employing indole and phenoxazine as donors for efficient DSSCs. *Tetrahedron* **2014**, *70*, 6296–6302. [CrossRef]

21. O'Boyle, N.M.; Tenderholt, A.L.; Langner, K.M. cclib: A library for package-independent computational chemistry algorithms. *J. Comput. Chem.* **2008**, *29*, 839–845. [CrossRef] [PubMed]

22. Hay, P.J.; Wadt, W.R. Ab initio effective core potentials for molecular calculations. Potentials for potassium to gold including the outermost core orbitals. *J. Chem. Phys.* **1985**, *82*, 299–310. [CrossRef]

23. Batsanov, S.S. Van der Waals radii of elements. *Inorg. Mater. (Transl. Neorg. Mater.)* **2001**, *37*, 871–885. [CrossRef]

24. Alvarez, S. A cartography of the van der Waals territories. *Dalton Trans.* **2013**, *42*, 8617–8636. [CrossRef] [PubMed]

25. Pinzaru, S.C.; Falamas, A.; Dehelean, C.; Morari, C.; Venter, M. Double amino functionalized Ag nanoparticles as SERS tags in Raman diagnostic. *Croat. Chem. Acta* **2013**, *86*, 233–244. [CrossRef]

26. Gong, Q.; Shi, W.; Li, L.; Ma, H. Leucine aminopeptidase may contribute to the intrinsic resistance of cancer cells toward cisplatin as revealed by an ultrasensitive fluorescent probe. *Chem. Sci.* **2016**, *7*, 788–792. [CrossRef]

27. Al Mamunur Rashid, M.; Hayati, D.; Kwak, K.; Hong, J. Theoretical investigation of azobenzene-based photochromic dyes for dye-sensitized solar cells. *Nanomaterials* **2020**, *10*, 914. [CrossRef]

28. Jafari, A.; Ghanadzadeh, A.; Tajalli, H.; Yeganeh, M.; Moghadam, M. Electronic absorption spectra of cresyl violet acetate in anisotropic and isotropic solvents. *Spectrochim. Acta Part A Mol. Biomol. Spectrosc.* **2007**, *66A*, 717–725. [CrossRef]

29. Banik, S.; Hussain, S.A.; Bhattacharjee, D. Modified aggregation pattern of cresyl violet acetate adsorbed on nano clay mineral layers in Langmuir Blodgett film. *J. Photochem. Photobiol. A Chem.* **2018**, *353*, 570–580. [CrossRef]

30. Ostrowski, P.P.; Fairn, G.D.; Grinstein, S.; Johnson, D.E. Cresyl violet: A superior fluorescent lysosomal marker. *Traffic* **2016**, *17*, 1313–1321. [CrossRef]

31. Itoh, Y.; Nakashima, Y.; Tsukamoto, S.; Kurohara, T.; Suzuki, M.; Sakae, Y.; Oda, M.; Okamoto, Y.; Suzuki, T. N$^+$-C-H···O Hydrogen bonds in protein-ligand complexes. *Sci. Rep.* **2019**, *9*, 767. [CrossRef] [PubMed]

32. Oprea, C.I.; Girtu, M.A. Structure and electronic properties of TiO$_2$ nanoclusters and dye-nanocluster systems appropriate to model hybrid photovoltaic or photocatalytic applications. *Nanomaterials* **2019**, *9*, 357. [CrossRef] [PubMed]